

Hydrothermal activity along the slow-spreading Lucky Strike ridge segment (Mid-Atlantic Ridge): Distribution, heatflux, and geological controls

Escartin J. ^{1,*}, Barreyre T. ², Cannat M. ¹, Garcia R. ³, Gracias N. ³, Deschamps A. ⁴, Salocchi A. ⁵, Sarradin Pierre-Marie ⁶, Ballu V. ⁷

¹ Laboratoire de Géosciences Marines, IGP, CNRS UMR7154, Paris, France

² Woods Hole Oceanographic Institution, Woods Hole, MA, USA

³ VICOROB, University of Girona, Spain

⁴ Laboratoire Domaines Océaniques, CNRS & Université de Bretagne Occidentale, Brest, France

⁵ University of Modena and Reggio Emilia, Modena, Italy

⁶ EEP, IFREMER, Brest, France

⁷ Université de La Rochelle, La Rochelle, France

* Corresponding author : J. Escartin, email address : escartin.javier@gmail.com

Abstract :

We have reviewed available visual information from the seafloor, and recently acquired microbathymetry for several traverses across the Lucky Strike segment, to evaluate the distribution of hydrothermal activity. We have identified a new on-axis site with diffuse flow, Ewan, and an active vent structure ~1.2 km from the axis, Capelinhos. These sites are minor relative to the Main field, and our total heatflux estimate for all active sites (200–1200 MW) is only slightly higher than previously published estimates. We also identify fossil sites W of the main Lucky Strike field. A circular feature ~200 m in diameter located on the flanks of a rifted off-axis central volcano is likely a large and inactive hydrothermal edifice, named Grunnus. We find no indicator of focused hydrothermal activity elsewhere along the segment, suggesting that the enhanced melt supply and the associated melt lenses, required to form central volcanoes, also sustain hydrothermal circulation to form and maintain large and long-lived hydrothermal fields. Hydrothermal discharge to the seafloor occurs along fault traces, suggesting focusing of hydrothermal circulation in the shallow crust along permeable fault zones.

Highlights

► Two new active and two inactive hydrothermal sites at Lucky Strike segment. ► Hydrothermalism linked to focused melt supply and central volcano formation. ► Heatflux of new sites only ~10% of that of the Main Lucky trike field. ► Shallow crust flow along permeable faults and seafloor discharge along fault traces.

Keywords : hydrothermalism, mid-ocean ridge, heat flux, faulting, oceanic crust, Mid-Atlantic Ridge

1. Introduction and geological setting

Hydrothermal activity along mid-ocean ridges controls cooling of the oceanic lithosphere, and impacts its thermal structure and the processes operating there (e.g., magmatic emplacement, faulting, seismicity, diking and melt delivery to the seafloor). Understanding the distribution of hydrothermal activity and its nature is necessary to quantify the associated heatflux, its partition between diffuse and focus flow recognizable at the seafloor, and to evaluate the amount of cooling withno expression at the seafloor (e.g., conductive cooling or low-temperature, diffuse percolation). Slow spreading ridge sections with significant melt supply typically define linear ridge segments with lengths of a few tens of km to up to ~100 km. These segments typically develop ridge-parallel normal faults on both flanks, and thick crust at their center indicating melt-focusing along-axis. As in the case of the Lucky Strike segment, sustained volcanism may lead to the development of central volcanoes (Escartín et al., 2014). The slow-spreading Lucky Strike segment is unique in that it has been extensively studied during more than two decades, following the discovery of the Lucky Strike hydrothermal field, from hereon referred to as the Main Lucky Strike hydrothermal field (MLSHF), located at its segment center and at the summit of the central volcano (Langmuir et al.,

61 1997). This is one of the most extensive hydrothermal fields discovered to date, and it is
62 located along a recent graben dissecting the Lucky Strike central volcano(Humphris et
63 al., 2002; Ondréas et al., 2009; Barreyre et al., 2012; Escartín et al., 2014). Water-column
64 studies have also revealed hydrothermal plumes at greater depths than that of the
65 MLSHF (Wilson et al., 1996; German et al., 1996; Thurnherr et al., 2008). These authors
66 proposed a yet unidentified source at the southern end of the segment and at a depth of
67 2000 m.

68 A ~3-3.5 km deep magma chamber(Singh et al., 2006)at the base of a ~600 m thick
69 Layer 2A (Seher et al., 2010) underlies The MLSHF (Figure 2). Major faults within the rift
70 valley(Escartín et al., 2014) can be linked to fault reflectors that do not reach the magma
71 chamber depth in seismic reflection profiles(Combi et al., 2015).Microseismicity
72 below the hydrothermal field(Crawford et al., 2013)is unrelated to these fault reflectors,
73 and likely corresponds to hydrothermal cooling instead (Figure 3).

74 In this paper we provide a synthesis of available information along the Lucky Strike
75 ridge segment, from seafloor observations and imagery to microbathymetricand
76 acoustic data (Figure 1).We analyze these data to identify and map new hydrothermal
77 sites, and use other observables (presence of a magma chamber, microseismicity,
78 faulting) to constrain the processes controlling distribution and location of hydrothermal
79 activity along this segment, to evaluate heat fluxes at the segment scale, and to discuss
80 the implications for heat extraction and magmatic supply. Finally, we review evidence of
81 hydrothermal activity along the segment based on water-column studies.

82

83 **2. Data and indicators of hydrothermal activity at the seafloor**

84 The Lucky Strike area has been targeted by numerous cruises in the last 25 years,
85 providing extensive visual information from direct human observations, video imagery,
86 and electronic still-camera images acquired with human-operated vehicles (HOVs),
87 remotely operate vehicles (ROVs), and deep-towed camera systems. These visual
88 observationsare complemented with near-bottom high-resolution bathymetry data
89 acquired both with ROVs and Autonomous Underwater Vehicles (AUVs) during cruises
90 in 2008 and 2009, in addition to a prior deep-towed sonar survey (Scheirer et al., 2000;
91 Humphris et al., 2002; Escartín et al., 2014), as summarized inFigure 1 and
92 Supplementary Table 1.Near-bottom ROV and AUV bathymetry data have a resolution of
93 several decimeters to a few meters per pixel, depending on survey altitude, and provide

94 detailed information on theseafloor texture that can be used to discriminate between
95 hydrothermal structures (e.g., hydrothermal mounds and chimneys, Figure 2) from
96 other structures whose origin is instead volcanic (e.g., hummocks, lava channels and
97 flows), tectonic (e.g., faults, fissures), or related to secondary mass-wasting processes
98 (e.g., landslides along fault scarps).

99 *2.1. Visual observations*

100 The bulk of the field work involving visual observations at the seafloor focuses on the
101 MLSHF, which is yearly visited since 2008 (MoMAR08) and is instrumented for
102 monitoring since 2010 as part of the MOMARSAT European Multidisciplinary Seafloor and
103 water column Observatory (EMSO) deep-sea seafloor observatory (Colaço et al., 2011).
104 In this study we use imagery and visual observations along with HOV, ROV, and deep-
105 towed camera systems (Figure 1a) that extend both along the Lucky Strike segment, and
106 across the full rift valley width (Figure 1a), and present a large-area seafloor
107 photomosaics from vertically-acquired imagery. The first systematic survey of the
108 MLSHF was conducted with ARGO II towed-camera in 1996 (Humphris et al., 2002;
109 Escartin et al., 2008). Subsequent surveys conducted with the ROV VICTOR low-light
110 camera covered fully the MLSHF (Barreyre et al., 2012), extending beyond prior surveys,
111 and South along the ridge axis (Figure 1). Vertical imagery was processed into a single
112 georeferenced seamless giga-mosaic. Details on the ARGO II and OTUS image surveys at
113 MLSHF, and on image processing and mosaicing are provided elsewhere (Escartín et al.,
114 2008; Barreyre et al., 2012; Prados et al., 2012); here we present for the first time the
115 2009 photomosaic ~1 km south of the MLSHF.

116 Active hydrothermal sites are readily identifiable visually from venting fluids (high-
117 temperature black smokers and clear-fluid vents, diffuse outflow at lower
118 temperatures), hydrothermal macrofauna and microbial communities (e.g., bacterial
119 mats and mussel beds), or white anhydrite deposits that require venting temperatures of
120 120-150°C (Bischoff and Seyfried, 1978). These visual features have been used to
121 extensively map the MLSHF from both photomosaics and oblique-view imagery acquired
122 with ROVs or HOVs (Barreyre et al., 2012). Fossil hydrothermal outflow areas are also
123 recognizable by fossil chimneys, sulfide rubble, and hydrothermal staining, which are
124 clearly distinguishable from basalt or sediment (Lalou et al., 1989; Barreyre et al., 2012).

125 Supplementary Table 1 and Figure 1 provide an overview of the seafloor visually
126 explored along >900 km of submersible tracks at the Lucky Strike segment, largely
127 concentrated at the segment center and the MLSHF. The seafloor photomosaics

128 (Barreyre et al., 2012) image ~ 1.5 km² of seafloor centered on the MLSHF, and ~ 0.4
129 km² on-axis ~ 2 km south of MLSHF. Seafloor observations outside the MLSHF were
130 conducted primarily during the 1994 DIVA cruise (Fouquet et al., 1994; Ondreas et al.,
131 1997) with both HOV Nautille and Scampi camera tows to the North, during the 2006
132 Graviduck cruise (HOV and camera tows), and during ROV dives in subsequent cruises
133 (Supplementary Table 1). In this paper the visual indicators of hydrothermal activity are
134 from shipboard observations (cruise reports and published results), and from a
135 systematic review of ROV and HOV video imagery and seafloor photography available to
136 us (cruises underlined in Supplementary Table 1).

137

138 *2.2. Microbathymetric data*

139 Microbathymetric data acquired in 2006 (MOMARETO cruise, Supplementary Table
140 1) (Ondreas et al., 2009), was complemented with MOMAR'08 and Bathyluck'09 surveys
141 using ROV VICTOR6000 equipped with a RESON 7150 multibeam system, and AUV
142 Aster-X equipped with a SIMRAD EM2000 multibeam system. After data processing
143 (ping editing, correction of navigation, filtering, and gridding), the final
144 microbathymetric grids have a pixel resolution that varies between 25 cm and 2 m per
145 pixel depending on survey altitude.

146 The MOMAR'08 and Bathyluck'09 surveys were conducted at the segment center and
147 over the central volcano summit, across the rift valley floor at different locations along
148 the segment, and at the flank of the southwestern inside corner of the segment end
149 (Figure 1). The combined set of microbathymetric surveys, which cover ~ 35 km² of the
150 Lucky Strike segment seafloor, is one of the most extensive microbathymetry surveys
151 along a slow-spreading ridge segment, and complements a prior ~ 190 km² high-
152 resolution sonar survey (Scheirer et al., 2000a; Escartín et al., 2014). For this study we
153 analyzed shaded relief and slope maps of the microbathymetric dataset to identify the
154 seafloor morphology consistent with that of hydrothermal deposits, as described below.

155

156 *2.3. Acoustic backscatter data*

157 The central portion of the Lucky Strike segment was surveyed with the DSL120 deep-
158 towed, near-bottom high-resolution sonar system (Scheirer et al., 2000; Humphris et al.,
159 2002). These data have been re-processed and presented elsewhere (Escartín et al.,
160 2014), together with an interpretation of the tectonic and volcanic structure of this

161 portion of the Lucky Strike segment. Sonar data are shifted locally to match the
162 microbathymetry, as the navigation of the DSL120 towed vehicle is less accurate than
163 that of ROV or AUVs used in microbathymetric surveys. By themselves sonar data are
164 not sufficient to identify hydrothermal deposits. First, sulfides do not display acoustic
165 properties that are distinct from basaltic basemen.. Second, acoustic backscatter
166 depends on numerous parameters such as insonification direction and angle, acoustic
167 shading, sedimentation, and instrumental artifacts, among other factors. In this study we
168 only use acoustic backscatter to support the interpretation of the microbathymetric data.

169

170 *2.4. Identification and extent of hydrothermal sites and fields*

171 Hydrothermal activity with high-temperature fluid discharge ubiquitously displays
172 mounds and chimneys that can reach up to a few tens of meters above surrounding
173 seafloor, with basal widths of meters to a few tens of meters (Figure 2). Areas with
174 hydrothermal vents have a characteristic microbathymetric signature, with spikes and
175 small-scale lumps, that corresponds to the “lumpy” seafloor morphology described
176 previously for the MLSHF(Ondreas et al., 2009) (Figure 2a), and for other hydrothermal
177 fields along mid-ocean ridges (Ferrini et al., 2008; Jamieson et al., 2014) elsewhere
178 (Figure 2b). This lumpy terrain can be clearly differentiated from the volcanic seafloor
179 morphology (hummocks, lava flows, lava channels) that tends to be spatially larger
180 structures (tens to hundreds of m) and that displays instead a smooth seafloor
181 morphology lacking spikes.

182 Zones with rubble, which are systematically found along slopes of fault scarps or
183 volcanic structures, show instead a granulated texture due to individual rock blocks,
184 which are systematically smaller than hydrothermal structures (~1-2 m or less, Figure
185 2a). This hydrothermal seafloor texture, which is common to hydrothermal fields (e.g.,
186 Lau Basin, Figure 2b)(Ferrini et al., 2008; Jamieson et al., 2014), is used here to map the
187 extent of hydrothermal sites within a hydrothermal field, or of new hydrothermal
188 fields.High-resolution acoustic backscatter, which can reveal this ‘lumpy’ hydrothermal
189 terrain under optimal insonification conditions, is used to complement the
190 microbathymetry.

191 Imagery(Figure 1a) is critical to confirm that sites identified in the microbathymetry do
192 correspond to hydrothermal deposits, active or inactive. It is also required to map areas
193 of diffuse hydrothermal outflow, young hydrothermal activity, or fossil structures, with

194 no clear morphological signature (bacterial mats, vents, hydrothermal staining, dead
195 chimneys, etc.). Extensive seafloor photomosaics are available for the MLSHF, where the
196 hydrothermal activity has been extensively mapped (Barreyre et al., 2012), and
197 additional photomosaics are available for an area ~2 km south of this site, along the
198 ridge axis (Figure 1a). The rest of the imagery is acquired along HOV, ROV, or tow tracks
199 (Figure 1a), which is adequate to identify areas of hydrothermal activity but cannot be
200 used to properly constrain the extent and limits of these areas.

201 Hence, the areas of 'lumpy' hydrothermal terrain identified in this study, based on
202 microbathymetric data (Figure 1b), indicate zones of significant and sustained
203 hydrothermal activity with significant sulfide accumulation. The bathymetric data also
204 reveal numerous volcanic features (hummocks, volcanic cones), tectonic structures
205 (fault scarps and fissures), and mass wasting indicators (slump scars, debris flows, scree,
206 dejection cones).

207 Water column studies have also been used to identify hydrothermal activity. High-
208 temperature black smoker type fluids form buoyant plumes in the water column that
209 can be detected from turbidity and manganese anomalies (Klinkhammer et al., 1985;
210 Baker et al., 2001; Baker, 2007; German et al., 2010), while methane anomalies can be
211 associated with sites showing both high-temperature venting (Lupton, 1990) and low-
212 temperature serpentinization (Bougault et al., 1993; Charlou and Donval, 1993; Gràcia et
213 al., 2000). The observations and datasets (microbathymetry, imagery, water column
214 studies) available along the Lucky Strike segment show thus limitations in the ability to
215 detect diffuse and very low-temperature outflow or conductive cooling, that are not
216 associated with either sulfide mounds (Figure 2) or with visual indicators of
217 hydrothermal activity (bacterial mats, anhydrite and other hydrothermal mineral
218 deposits).

219

220 **3. Hydrothermal sites at the Lucky Strike segment**

221 Based on both the imagery and the microbathymetry shown in Figure 1, we have
222 characterized the distribution and nature of hydrothermal discharge throughout the rift
223 valley floor of the Lucky Strike segment. The distribution of hydrothermal activity and
224 deposits of the Main Lucky Strike hydrothermal field have been mapped in recent
225 studies (Ondréas et al., 2009; Barreyre et al., 2012). Using the new microbathymetric
226 data we have identified additional hydrothermal deposits at the western edge of

227 this main hydrothermal field and extended its limits (Figure 3, Table 1). We also report
228 three additional hydrothermal sites along the Lucky Strike segment (Figure 3). Two out
229 of these three new sites, Ewan and Capelinhos, have been visited and are confirmed to be
230 active. The third site at the MLSHF has been visited and confirmed to be inactive (H6;
231 Figure 4). The fourth site, Grannus, has been identified solely from the microbathymetric
232 seafloor texture, but lacks direct visual observations to determine if it is active or
233 inactive, or what may be the nature of the associated hydrothermal deposits.

234

235 *3.1. Main Lucky Strike hydrothermal field (MLSHF)*

236 The MLSHF has been systematically mapped and studied during the last two decades
237 since its discovery in the 90's (Supplementary Table 1) (Langmuir et al., 1997; Humphris
238 et al., 2002; Escartín et al., 2008; Ondréas et al., 2009; Barreyre et al., 2012; Barreyre et
239 al., 2014b; Mittelstaedt et al., 2012). Microbathymetry acquired during the Momareto'06
240 survey has been used to identify the extent, nature, and limits of several areas
241 corresponding to hydrothermal deposits and associated debris (1 through 4 in Figure 3,
242 Table 1). This morphological mapping is complemented by large-area seafloor
243 photomosaics (Escartin et al., 2008; Barreyre et al., 2012; Mittelstaedt et al., 2012;
244 Prados et al., 2012), used to determine the distribution of both fossil and active venting
245 (Barreyre et al., 2012) both within these hydrothermal areas and elsewhere throughout
246 the field (Figure 3).

247 The data collected during the MOMAR'08 and Bathyluck'09 cruises reveal two new
248 hydrothermal areas at the MLSHF (Areas 5 and 6 in Figure 3). Area 5, which is located in
249 the southwestern part of the MLSHF and within the axial graben (Figure 3, Table 1), is
250 associated with zones of diffuse flow and scattered active and inactive vents that are
251 visible in the microbathymetry.

252 Area 6 is located ~1.5 km from the center axis at the western edge of the MLSHF, and in
253 the immediate vicinity of the main fault scarp bounding the axial graben. The seafloor in
254 this area, which corresponds to the flank of an axial volcano recently rifted, is cross-cut
255 by small-scale normal faults with vertical displacements of up to a few meters, and with
256 'lumpy' hydrothermal seafloor texture (Figures 3, 4). Area 6a corresponds to a broad
257 mound with several spikes (vents) extending over an area of ~70x70 m (Figure 4), and
258 that buries a normal fault scarp that is visible towards the North. Areas 6b and 6c, which
259 had been previously identified in microbathymetric data (Ondréas et al., 2009), are

260 smaller and show instead several isolated spikes and no clear mound. Observations from
261 VICTOR#605 dive (MOMARSAT'15 cruise, Figure 4) found no evidence of active
262 hydrothermal activity, but confirmed that the pinnacles correspond to fossil
263 hydrothermal chimneys (Figure 4c), and that the area displays numerous indicators of
264 fossil hydrothermal outflow such as smaller hydrothermal mounds (Figure 4d),
265 hydrothermal staining, sulfide rubble, shell chaff, and hydrothermal slab similar to that
266 found at the center of the MLSHF.

267 3.2. Ewan

268 The Ewan hydrothermal field was serendipitously discovered during HOV Nautilie dive
269 1624 (Graviluck 2006 cruise, Supplementary Table 1). This dive crossed a series of
270 seafloor patches covered with filamentous bacterial mats that are white and highly
271 reflective when illuminated, associated with mussel beds, and primarily found along
272 scarps and slopes covered with rubble and sediment (Figure 5a-c). Following its
273 discovery, the site was fully surveyed to obtain seafloor photomosaics and
274 microbathymetry (Figures 5d-g, MOMAR'08 and Bathyluck'09 cruises, Supplementary
275 Table 1). Ewan is located within the axial graben dissecting the central volcanic
276 cone (Escartín et al., 2014), ~2 km south of the MLSHF (Figures 3 and 5f). The seafloor
277 here displays a complex set of horst and graben (Figure 5f), with numerous east- and
278 west-verging normal faults that confine the most recent, unsedimented lava
279 flows (Escartín et al., 2014).

280 In the photomosaics bacterial mats correspond to white areas with a mottled seafloor
281 aspect (Figures 5c-d), with irregular and gradational limits. Owing to the resolution of
282 the photomosaics (5-10 mm per pixel), we can also identify macrofauna associated with
283 the vents (e.g., fish, Figure 5e), but mussel beds associated with the bacterial mats are
284 not visible in this imagery. Using mapping techniques and interpretation developed
285 earlier (Barreyre et al., 2012), we identified and digitized ~150 larger patches, in
286 addition to >400 that are too small to be digitized, and for which we only record their
287 position. The ~150 digitized patches cover ~275 m², while the rest correspond to ~30
288 m², attributing 0.06 m² to each of the smaller features (~0.25x0.25 m²). These estimates
289 (Table 2) are likely minima as topography is not accounted for (flat projection), and the
290 photomosaic have gaps where active areas may occur.

291 Ewan contains several clusters of bacterial mats along a NNE-SSW direction, extending
292 ~250 m along-axis and ~40 m across axis, and in the continuation of aligned pits ~10 m
293 deep and ~30 m wide (Figure 4g). Bacterial mats occur both along slopes (pits, fault

294 scarps, Figure 5a-c) and flat-lying, volcanic seafloor (ropy lavas, RL, in Figure 5d).
295 Detailed HOV observations (Figure 3c) revealed shimmering locally, as observed in
296 diffuse outflow areas at the MLSHF. We did not find active nor fossil high-temperature
297 venting (e.g., active or fallen chimneys) during the HOV dive or in the seafloor
298 photomosaics, suggesting that Ewan hosts only diffuse hydrothermal activity. The
299 distribution and shape of individual bacterial patches also indicates fluid percolation
300 through the seafloor at very slow flow rates.

301

302 *3.3. Capelinhos*

303 Capelinhos is a vent field located ~1.5 km E of the MLSHF, on the western, outward-
304 dipping flank of a summital volcanic cone (Figures 3 and 6) first identified in the
305 microbathymetric data (Bathyluck'09 cruise). The site was first visited during an ROV
306 dive in 2013 (MoMARSAT'13 cruise, Supplementary Table 1), which confirmed its
307 activity. The microbathymetry shows a main hydrothermal mound that peaks ~20 m
308 above the surrounding seafloor, centered along the trace of a small fault scarp and
309 fissure now buried by the hydrothermal deposits (Figure 6d). This hydrothermal edifice,
310 which links with nearby structures that rise a few meters to 10 m above surrounding
311 seafloor (Figure 6d), shows a low acoustic backscatter and lacks any clear texture in the
312 sonar imagery (Figure 6e). ROV dives (Figure 6d) have confirmed the presence of both
313 inactive and active chimneys with high-temperature outflow through black smokers,
314 clear vents, and flanges (Figure 6a-c). Visual observations suggest that diffuse flow is
315 limited at this site, but we lack seafloor photomosaics to accurately evaluate the type,
316 geometry, and distribution of diffuse flow as done for Ewan and the MLSHF.

317 At a distance of 150 m to the southwest of the Capelinhos vent the bathymetry shows a
318 ~50 m diameter dome rising ~2-3 m above surrounding seafloor, which has not been
319 visited to date (Figure 6d). Nearby fissures immediately to the north expose layered
320 deposits, reminiscent of hyaloclastite layers blanketing the MLSHF (Ondreas et al., 1997;
321 Ondreas et al., 2009). This structure is located in the immediate vicinity of the fault
322 buried by Capelinhos, and its associated acoustic backscatter is low and the sonar
323 featureless, as observed for the main vent structure (Figure 6e). A hydrothermal origin
324 is inconsistent with its surface morphology, which lacks the typical 'spikes' found in
325 hydrothermal terrain. Irregular terrain found East of Capelinhos is instead of volcanic
326 origin (Figures 6d and e). ROV observations in the area show a sedimented seafloor with
327 pillows visible locally, with no evidence of standing hydrothermal chimneys or mounds,

328 and possible hydrothermal staining that is local and minor, and that has not been
329 sampled. The associated sonar imagery shows a hummocky volcanic texture that is
330 common along the axial seafloor of the Mid-Atlantic Ridge (Smith and Cann, 1990; Yeo et
331 al., 2011).

332

333 *3.4. Grunnus*

334 Microbathymetric data and sonar imagery show a possible off-axis hydrothermal field,
335 named Grunnus (Figure 7), ~2.5 km west of the MLSHF and corresponding to a
336 spreading age of ~220 kyrs (Table 1). This structure has a diameter of ~200 m, with
337 steep flanks, and a platform ~40-50 m above the surrounding seafloor to the S, and that
338 abuts against the coalescing volcanic cones and hummocks on the flanks of the rifted
339 central volcano to the north. This platform hosts a 20-m high structure that casts a clear
340 shadow in the sonar imagery towards the E (Figure 7b). The shape and size of Grunnus
341 is reminiscent of that of the TAG hydrothermal mound, which has a pancake shape ~200
342 m in diameter and ~50 m in height (Humphris and Kleinrock, 1996). Microbathymetry
343 and the sonar data show by small-scale rugosity and pinnacles at its surface that we
344 attribute to hydrothermal structures (chimneys, mounds). The volcanic mounds to the
345 north display instead a smooth surface (Figure 7).

346 While the mound at Grunnus has not been visited, we suggest that this off-axis site is
347 likely inactive. Observations during an HOV dive conducted in 2006 (Graviluck'06 cruise,
348 Figure 7a) that approached the base of Grunnus yielded no evidence of hydrothermal
349 deposits, activity, nor indicators of present or past fluid flow. Furthermore, water
350 column studies nearby (Wilson et al., 1996; Thurnherr et al., 2008) lack a hydrothermal
351 plume signature, and seismic reflection and refraction data (Singh et al., 2006; Crawford
352 et al., 2010; Combi et al., 2015) do not image an underlying AMC that may act as a heat
353 source for an active hydrothermal field.

354 Bathymetry and sonar imagery also show a fault cross-cutting the western flank of the
355 mound. The fault scarp is well defined and sharp towards the southwest of the mound,
356 where it shows up to ~5 m of vertical throw and crosscuts seafloor lacking
357 hydrothermal texture. Across the mound this fault scarp is recognizable but is not as
358 well-defined, suggesting that deformation postdated mound emplacement and growth.
359 The difference in fault morphology and height between the mound and surrounding

360 seafloor may be attributed to the different mode of faulting in poorly consolidated
361 hydrothermal deposits relative to basaltic seafloor.

362

363

364 **4. Discussion**

365 *4.1 Magmatic controls on distribution of hydrothermal activity*

366 The review and analysis of seafloor imagery and microbathymetric data along the Lucky
367 Strike segment (Figure 1) has allowed us to map new areas with fossil hydrothermal
368 deposits at the western edge of the MLSHF. The location of the four sites at the segment
369 center, and the lack of any visual or bathymetric indicators of hydrothermal activity
370 elsewhere along the segment, suggest a link between melt focusing to the segment center
371 and heat sources stable over long periods of time generating hydrothermal activity. Our
372 results do not preclude hydrothermal activity elsewhere, that would be undetected in
373 the absence of visual imagery (diffuse venting with no morphologic signature), in areas
374 imaged but lacking detailed observations to detect low-temperature flow that is not
375 associated with bacterial mats or anhydrite deposits, or in areas where no near-bottom
376 data exists (see section 4.4. for discussion of water column studies).

377 Of the three active fields, MLSHF and Ewan are at the summit of the central volcano,
378 along the axial graben dissecting it (Ondréas et al., 2009; Escartín et al., 2014), and
379 immediately above the ~3-3.5 km deep axial magma chamber (AMC) (Singh et al., 2006;
380 Combier et al., 2015). The AMC is not centered at the present-day ridge axis, and both
381 Ewan and MLSHF are located towards its eastern edge, while Capelinhos is located ~700
382 m east of the AMC's edge (Figure 3 and 8). The AMC also extends ~6 km along-axis,
383 likely imparting a three-dimensional thermal structure where temperature gradients
384 can focus flow towards the segment center (Fontaine et al., 2011).

385 The off-axis Grunnus field is on a volcano flank originally emplaced at the Lucky Strike
386 segment center and since rifted. The original setting is thus similar active on- and near-
387 axis fields along this segment (MLSHF, Ewan, and Capelinhos, Figure 3). It is likely that,
388 as in the case of the hydrothermally active segment center, the Grunnus field may have
389 been animated by a magma chamber underlying the rifted central volcano at the time of
390 its formation, both now extinct.

391

393 *4.2 Faulting, permeability structure, and outflow at the seafloor*

394 Figure 8 presents a schema of fluid flow within the upper crust associated with the
395 active hydrothermal fields at the active Lucky Strike hydrothermal field, based on
396 geological observations and geophysical data. First, the permeability of the crust
397 immediately above the AMC is likely lower than that of the shallow crust Layer
398 2A(Barreyre et al., 2014a)owing to its composition and the confining pressure(Figure 8).
399 This crustal section must host the hydrothermal upwelling animated by the presence of
400 the AMC, likely to be distributed and in the form of broad hydrothermal plumes of up to
401 1 km in diameter for reasonable crustal permeabilities (Fontaine et al., 2014), as shown
402 in Figure 8.

403 Second, fluid flow at the seafloor is not broadly distributed, but localized along or
404 nearfaults. This has been welldocumented for individual vents and areas of diffuse flow
405 within the MLSHF through detailed hydrothermal and tectonic mapping (Barreyre et al.,
406 2012), and for the newly discovered active sites. Ewan is set on tectonic depressions
407 within the axial graben (Figure 5), while the Capelinhos edifice and associated
408 structures are set at the continuation of fault traces visible in surrounding seafloor
409 (Figure 6), covered subsequently by hydrothermal deposits. This association between
410 hydrothermal outflow and faults, widely observed at other deep-sea hydrothermal fields
411 at all spreading ridges and in different tectonic environments(Kleinrock et al., 1993;
412 Haymon et al., 2005; Pedersen et al., 2010; Marcon et al., 2013),suggests that permeable
413 faultschannel hydrothermal flow in the shallow crust(Barreyre et al., 2012; Barreyre et
414 al., 2014a), as illustrated in Figure 8.

415 Rifting and diking at the Lucky Strike segment center have concentrated along the ~1
416 km-wide axial graben dissecting the Lucky Strike central volcano(Humphris et al., 2002;
417 Ondréas et al., 2009; Escartín et al., 2014). These processes may play an important role
418 in the permeability of the crust overlying the AMC, with the development of a zone of
419 high-permeability following the axial graben, and induced by thermal cracking and
420 fracturing associated with dike emplacement, and by small-scale faulting that is likely
421 limited to the shallowest 1-2 km of the crust (Figure 8). An anisotropic permeability
422 structure, coupled with a magma chamber, can promote along-axis convection cells
423 (Fontaine et al., 2014) consistent with microseismicity clusters observed here above the
424 AMC (Crawford et al., 2013), with clusters resulting from cracking-induced
425 microseismicity induced by cooling. It is thus likely that the two microseismicity clusters

426 along the axial graben, one immediately north of the MLSHF, and the second below the
427 summit of the axial volcanic cone (Figure 3) correspond to cooling in downflow
428 areas. Venting at Capelinhos, which is East of the AMC edge, is then likely associated to
429 flow along a permeable fault that may root at the main upwelling zone and below the
430 Layer 2A (Figure 8). Ewan may correspond instead to a minor axial upwelling relative
431 the MLSHF, and associated with a downwelling area below the rifted axial volcano
432 located between these two hydrothermal fields (Figure 3). Alternatively, Ewan may be
433 associated with a recent magmatic event such as the emplacement of a lava flow or dike
434 propagation in the shallow crust as suggested by hydrophone data (Dziak et al., 2004).

435 *4.3 Revised hydrothermal heat flux at Lucky Strike*

436 The new observations and results presented here allow us to update the heat flux
437 estimates of known hydrothermal activity at the Lucky Strike segment (Ewan and
438 Capelinhos in addition to MLSHF), based on visual and instrumental observations. A
439 prior estimate of heatflux for MLSHF, based on the photomosaic and a systematic
440 evaluation of the distribution of vents, yielded values of 195-1086 MW (Barreyre et al.,
441 2012). As the only new hydrothermal area within this field found in this study is inactive,
442 this estimate remains unchanged.

443 Ewan displays only diffuse and low-temperature hydrothermal discharge, that we have
444 fully mapped using the seafloor photomosaics (Figure 5). Adopting the methodology of
445 Barreyre et al. (2012), we estimate the minimum and maximum heatflux based on the
446 area of diffuse outflow estimated from the photomosaics (Figure 3), and the estimated
447 temperature and velocity of the outflow from studies in similar settings (see details in
448 Barreyre et al., 2012, and Table 2). We obtain a heatflux estimate that ranges from 4.4-
449 117 MW. In our calculations we likely underestimate the surface of diffuse outflow, as it
450 is calculated over images projected to a horizontal plane without taking into account the
451 steep topography present in the area (Figure 5). As in the case of the MLSHF diffuse
452 fluxes, other uncertainties are the velocity and the temperature of the diffuse outflow,
453 which are not constrained by systematic measurements at this site. Visual inspection of
454 the Capelinhos site shows that there are two active main chimneys with a total of ~10-
455 15 vents identified (Figure 4), in addition to flanges with diffusers. Assuming a total of
456 10-20 vents with a heatflux of 0.12-0.8 MW/vent (Barreyre et al., 2012; Mittelstaedt et al.,
457 2012) we estimate the Capelinhos heat-flux at 1.2-16 MW.

458 The hydrothermal heat flux that we estimate for the new active sites (5.6-133 MW, Table
459 2) are thus minor relative to the 195/1086 MW previously reported for the MLSHF

460 (Barreyre et al., 2012). This represents an increase of ~10% in our heatflux estimate
461 that is taken up primarily by diffuse hydrothermal outflow (80-90% of the total heatflux,
462 Table 2), although the importance of diffuse outflow appears to vary greatly from site to
463 site (100% at Ewan and almost non-existent at Capelinhos).

464 *4.4 Water column anomalies and elusive hydrothermal plumes*

465 Water column studies throughout the Lucky Strike segment report anomalies attributed
466 to hydrothermal plumes rising from undiscovered fields, although their evidence is
467 elusive. Light transmission anomalies and elevated CH₄ concentrations south of the
468 MLSHF and central volcano (Wilson et al., 1996) have been attributed to an unidentified
469 but large field at ~2100 m (W in Figure 9). During the HEAT cruise (German et al., 1996),
470 TOBI deep-tow sonar detected one anomaly along the non-transform offset between
471 Lucky Strike North and Famous segments, and another one at the southern edge of the
472 nodal basin during a hydrographic cast (G in Figure 9). More recently, hydrographic
473 stations revealed a water column anomaly at 1800 m bsl at the southern segment
474 end (Thurnherr et al., 2008) (T in Figure 9). Finally, CH₄ anomalies indicating low-
475 temperature hydrothermal activity associated with serpentinization and not linked to
476 black smoker activity (lack of a manganese signature) have been identified at Menez
477 Hom (Gràcia et al., 2000), and at the southern inside-corner of the Lucky Strike
478 segment (Gr in Figure 9).

479 Numerous other hydrographic profiles conducted throughout this segment show no
480 water column anomaly. These including casts during the Gravituck cruise shown in
481 Figure 9 (Thurnherr et al., 2008), ROV dives during the cruises in 2008 and 2009 (Figure
482 9 and Supplementary Table 1), or deep-towed surveys using TOBI (German et al., 1996;
483 Gràcia et al., 1998), which detected no water column anomalies other than those along
484 the non-transform offset and the end of the segment (German et al., 1996) (Figure 9). In
485 many casts, the plume of the MLSHF is not detected (Figure 9), likely due to complex
486 hydrography and strong seafloor currents (Thurnherr et al., 2008) that may sweep or
487 dilute its plume. Furthermore, seafloor observations and microbathymetry surveys
488 available in the immediate proximity of some of these anomalies (Figure 9) provide no
489 evidence of activity away from the three active hydrothermal fields at the center of the
490 segment (Figure 3). Therefore the evidence for additional undiscovered hydrothermal
491 fields inferred along the southern portion of the Lucky Strike segment (Wilson et al.,
492 1996; German et al., 1996; Thurnherr et al., 2008) is weak owing to the unexplained
493 spatial and temporal inconsistencies of hydrographic data indicating the presence or

494 absence of hydrothermal plumes, the lack of visual or morphologic indicators of
495 hydrothermal activity away from the segment center, and the complex hydrography of
496 the area.

497 *4.5. Significance for hydrothermal activity along slow spreading segments*

498 Central volcanoes other than Lucky Strike host active vents. At intermediate-spreading
499 ridges, Axial Volcano along the Juan de Fuca Ridge is also underlain by a magma
500 chamber 2.5-3.5 km below seafloor, hosts several hydrothermal sites that are
501 monitored (Kelley et al., 2014). At slower-spreading ridges, the Menez Gwen
502 field (Ondreas et al., 1997; Marcon et al., 2013) and the Koberinsey field (Olafsson et al.,
503 1989) along the Mid-Atlantic Ridge, and the Soria Moria and Troll Wall along the Arctic
504 Ridges (Pedersen et al., 2010) all occur on central volcanoes at similar phases of rifting as
505 that of Lucky Strike, dissected at the summit by narrow and localized axial graben. It is
506 likely that these sites are also underlain by magma chambers linked to central volcano
507 formation, and such fields may be common at central volcanoes along ridge segments
508 (Escartín et al., 2014) that are yet unexplored.

509 Hydrothermal activity at central volcanoes is likely to be persistent over long periods of
510 time, continuously or intermittently, owing to sustained and enhanced melt supply
511 required for their formation. This is supported by the presence of both isolated
512 hydrothermal vents and areas of hydrothermal deposits that are inactive at Lucky Strike
513 (Area 5, Table 1), and by the off-axis Grunnus site on a rifted central volcano. While
514 there are no age constraints on hydrothermal deposits at the Main Lucky Strike
515 hydrothermal field (Figure 3), it is likely to have been active over thousands to a few tens
516 of thousands of years (Humphris et al., 2002; Barreyre et al., 2012). Other basalt-hosted
517 hydrothermal fields found along axial volcanic ridges (e.g., Broken Spur (Murton et al.,
518 1994; Murton et al., 1999), Snake Pit (Karson and Brown, 1988), BeeBee (Connelly et al.,
519 2012) or Lilliput (Haase et al., 2009)) are much smaller in size and probably with
520 shorter life-spans. These may be likely associated to short-lived heat sources (e.g., dike
521 intrusions or recent volcanic eruptions). The long-lived hydrothermal fields
522 associated with central volcanoes are likely to play a major role in the dispersion and
523 propagation along the ridge-axis of hydrothermal ecosystems and on the biogeography
524 of these communities (Van Dover et al., 2002).

525 **Conclusions**

526 Extensive seafloor imagery and visual observations together with microbathymetry
527 acquired with deep-sea vehicles have allowed us to evaluate the distribution of
528 hydrothermal activity at the scale of the Lucky Strike segment, and to re-evaluate the
529 associated heatflux. The Lucky Strike segment hosts three active hydrothermal fields:
530 The known MLSHF, Capelinhos, and Ewan. Capelinhos is located 1.3 km E of the axis and
531 the Main field, and consists of a ~20 m sulfide mound with black smoker vents. Ewan is
532 located ~1.8 km south from the Main LS field long the axial graben, and displays only
533 diffuse flow along and around scarps of collapse structures associated with fault scarps.
534 At the Main Lucky Strike hydrothermal field we have identified an inactive site, thus
535 broadening the extent of this field. Heat flux estimates from these new sites are relatively
536 low and correspond to ~10% of the heat flux estimated for the Main field, with an
537 integrated heatflux of 200-1200 MW. Overall, most of the flux (up to 80-90%) is
538 associated with diffuse flow, with the Ewan site showing solely diffuse flow and
539 Capelinhos mostly focused flow. The microbathymetry also reveals a large, off-axis (~2.4
540 km) hydrothermal field, comparable to the TAG mound in size, on the flanks of a rifted
541 volcano. The association of these fields to a central volcano, and the absence of
542 indicators of hydrothermal activity along the ridge segment, suggest that sustained
543 hydrothermal activity is maintained by the enhanced melt supply and the associated
544 magma chamber(s) required to build central volcanoes. In all cases hydrothermal
545 outflow at the seafloor is controlled by faults, indicating that these tectonic structures
546 are permeable and exploited by the hydrothermal circulation in the shallow crust. Our
547 observations, together with inconsistencies in available oceanographic data, also fail to
548 constrain the possible source(s) of all anomalies detected in water column. Central
549 volcanoes are thus associated with long-lived hydrothermal activity, and these sites may
550 play a major role in the distribution and biogeography of vent communities.

551

552

553 **Acknowledgements.** This work has been partly financed by ANR (France) Mothseim
554 Project NT05-3 42213 to JE, and by EU-RTN-MOMARNET to MC. The French Ministry of
555 Research financed ship, ROV and AUV time (Graviluck'06, MOMAR'08, Bathyluck'09,
556 MOMARSAT cruises in 2010-2015). *TowCam* deployment during Graviluck cruise was
557 supported by NSF grant OCE-0623744 to A. Soule and D. J. Fornari (WHOI, USA).

558 **Table 1.** Hydrothermal fields at the Lucky Strike ridge segment. The limit of sites H1 through H4 in the Main Lucky Strike field have been
 559 defined previously (Ondréas et al., 2009), as well the distribution of focused and diffuse hydrothermal outflow by (Barreyre et al., 2012). Sites
 560 H5 and H6 in the Main Lucky Strike Field, and the Ewan, Capelinhos, and Grunnus fields are described in this paper.
 561

<i>Name</i>	<i>Longitude</i>	<i>Latitude</i>	<i>Depth, m</i>	<i>Area, m²</i>	<i>Distance, km (spreading age, kyr)[#]</i>	<i>In situ data</i>	<i>Activity*</i>
Main Lucky Strike field					0-0.6 (0-53)	Visual, photomosaic	
H1	32°16.92'W	37°17.61'N	1620-1720	30304			Active, f+d
H2	32°16.50'W	37°17.48'N	1620-1670	35535			Active, f+d
H3-Eiffel Tower	32°16.52'W	37°17.33'N	1680	1506			Active, f+d
H3a	32°16.60'W	37°17.43'N	1670	5066			Active, f+d
H3b	32°16.62'W	37°17.37'N	1680-1700	3856			Active, f+d
H3c	32°16.52'W	37°17.27'N	1700	1454			Active, f+d
H4	32°16.90'W	37°17.41'N	1710	282			Active, f+d
H5	32°16.84'W	37°17.39'N	1725	10429			Active, f+d
H6a	32°17.08'W	37°17.71'N	1585	4479			Inactive
H6b	32°17.05'W	37°17.64'N	1590	2259			Inactive
H6c	32°17.07'W	37°17.69'N	1590	2597			Inactive
Ewan	32°17.27'W	37°16.61'N	1770	3010	0 (0)	Visual, photomosaic	Active, d
Capelinhos	32°15.83'W	37°17.35'N	1665	20712	1.4 (130)	Visual	Active, f (d)
Grunnus	32°18.25'W	37°18.02'N	1645	35704	2.4 (220)	None	Inactive?

584 Notes:#Distance is measured to centerline of axial graben, and spreading age calculated assuming a full spreading rate of 22 km/Myr. For the main
 585 Lucky Strike we report the minimum and maximum distances and the associated spreading ages.

586 *Activity of sites is confirmed visually except for Grunnus, which has not been visited to date. Type of flow: f - focused flow (vents); d - diffuse flow.
 587 Type of flow in parenthesis denotes minor occurrence.

588 **Table 2.** Ranges (min/max)? Heatflux estimates of Lucky Strike hydrothermal fields.
 589 Calculations are based on the number of high-temperature vents and surface of areas of
 590 diffuse flow identified visually (this study) and instrumental measurements (temperature,
 591 currents), following the methodology of Barreyre et al. (2012).

592 Ewan hydrothermal field (diffuse)

593 Large patches: S: 274 m² Q=4.2/92 MW
 594 Small patches: Number=1072; S: 11 m² Q=0.2/15 MW
 595 Total EWAN Q=4.4/117 MW

597 Capelinhos hydrothermal field (focused)

598 Vents Number= 10-20; Q/vent=0.12-0.8 MW Q=1.2/16 MW

600 Main Lucky Strike hydrothermal field (focused + diffuse)(Barreyre et al., 2012)

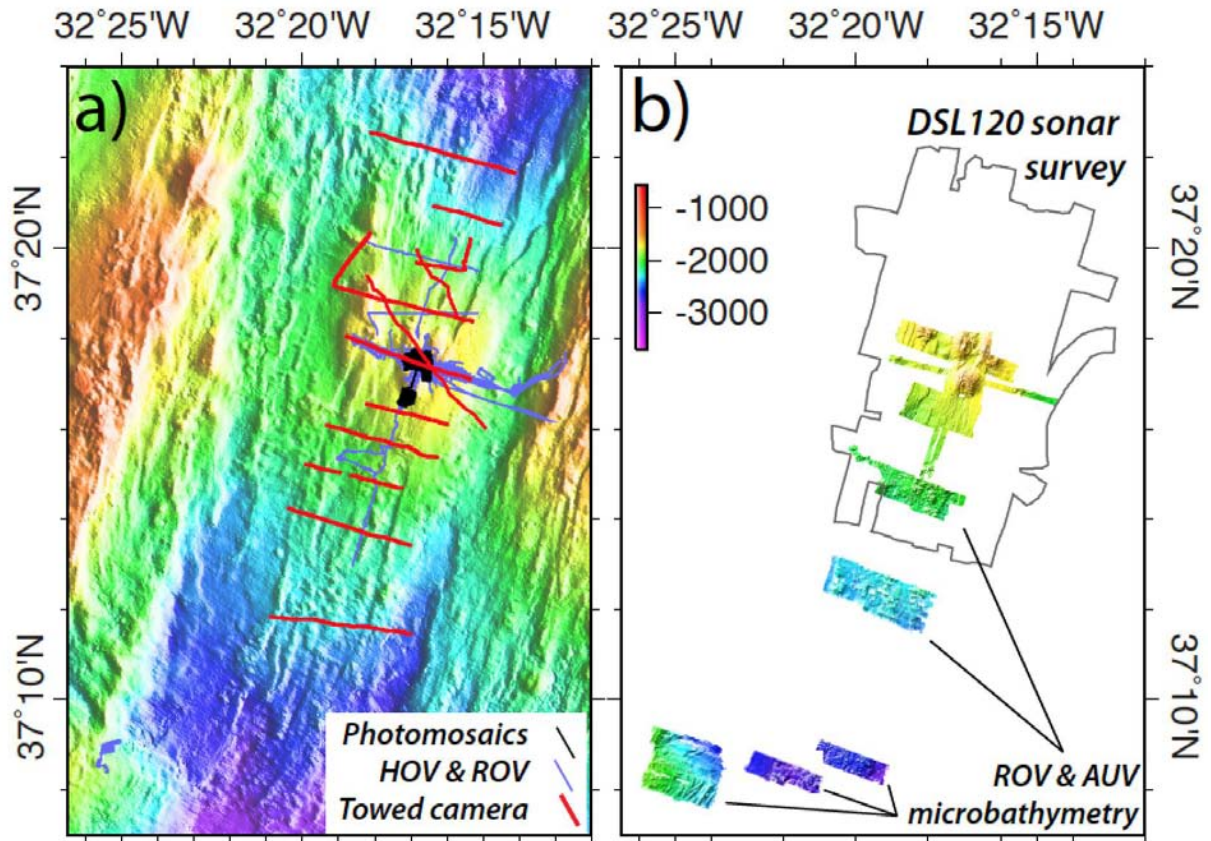
601 Diffuse flow Q=187/1036 MW
 602 Focused flow Q=8/50 MW
 603 Total MLSHF Q=195/1086 MW

605 Combined heat-fluxes at Lucky Strike

606 **Diffuse flow Q=191/1143 MW**
 607 **Focused flow Q=9/66 MW**
 608 **Total heatflux Q=200/1210 MW**

609 * Diffuse flow: $Q = \Delta T \times \phi \times v \times C_p \times S$, where ρ is density of seawater (1025 kg.m⁻³), C_p is the
 610 specific heat of the diffuse fluid (4.2 10³ J.kg⁻¹°C⁻¹), ΔT is temperature difference $T-T_0$ between
 611 outflow temperature T and ambient seawater T_0 (4.4°C), v is the diffuse effluent velocity, and S
 612 the area of considered diffuse outflow (m²). T minimum and maximum values are 8 and 20°C,
 613 and v minimum and maximum values are 1 and 5 mm/s, as described by Barreyre et al. (2012)
 614 and references therein. S is reported in the Table 1.

615 Focused flow: Individual vent heatflux is estimated at 0.12-8 MW, as described by Barreyre
 616 et al. (2012). The total heatflux associated to focused flow is the integration of the heatflux from
 617 individual vents, which are visually identified in available ROV video imagery.

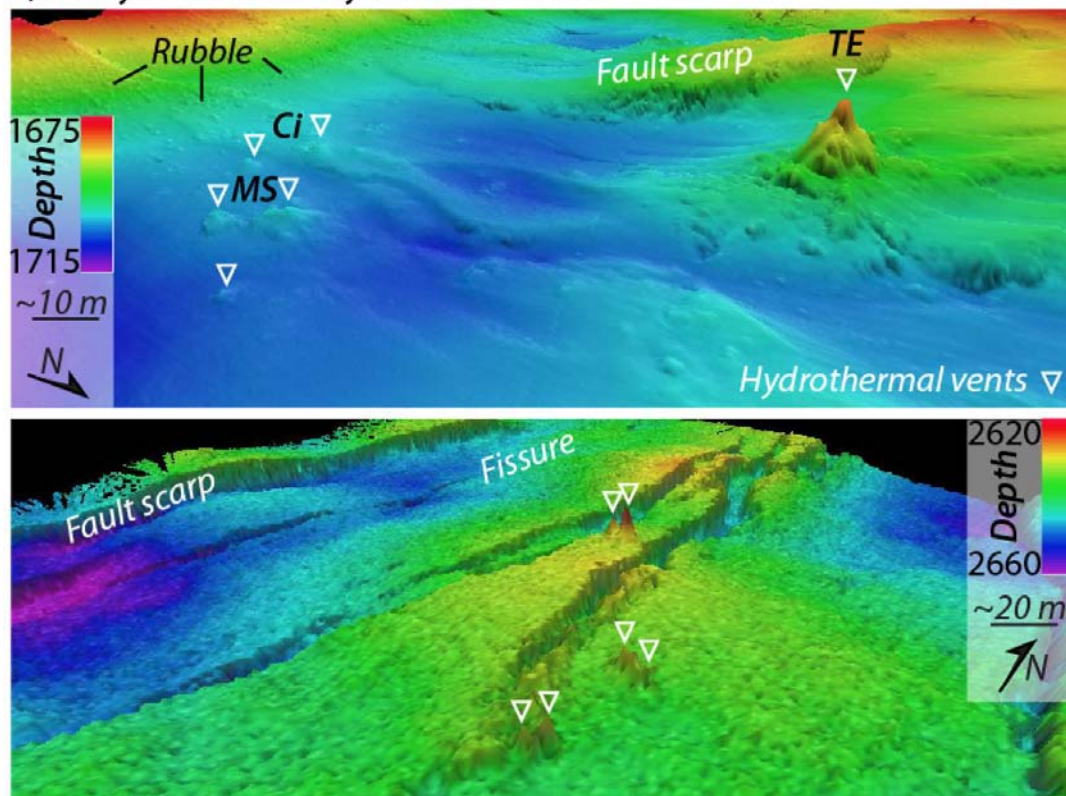


618

619

620 **Figure 1.** a) Visual information of the seafloor is available from ROV photomosaics, and
 621 along tracks of HOVs, ROVs, and deep-towed cameras. b) Available microbathymetric
 622 data from the Lucky Strike ridge segment, acquired during near-bottom ROV and AUV
 623 surveys (Momareto'06 and MOMAR'08 and Bathyluck'09 cruises). The outline of the
 624 DSL120 sonar survey, acquired during the Lustre'96 cruise, is also shown. See
 625 Supplementary Table 1 for additional details on these cruises, the deep-sea vehicles
 626 deployed, and types of data acquired.

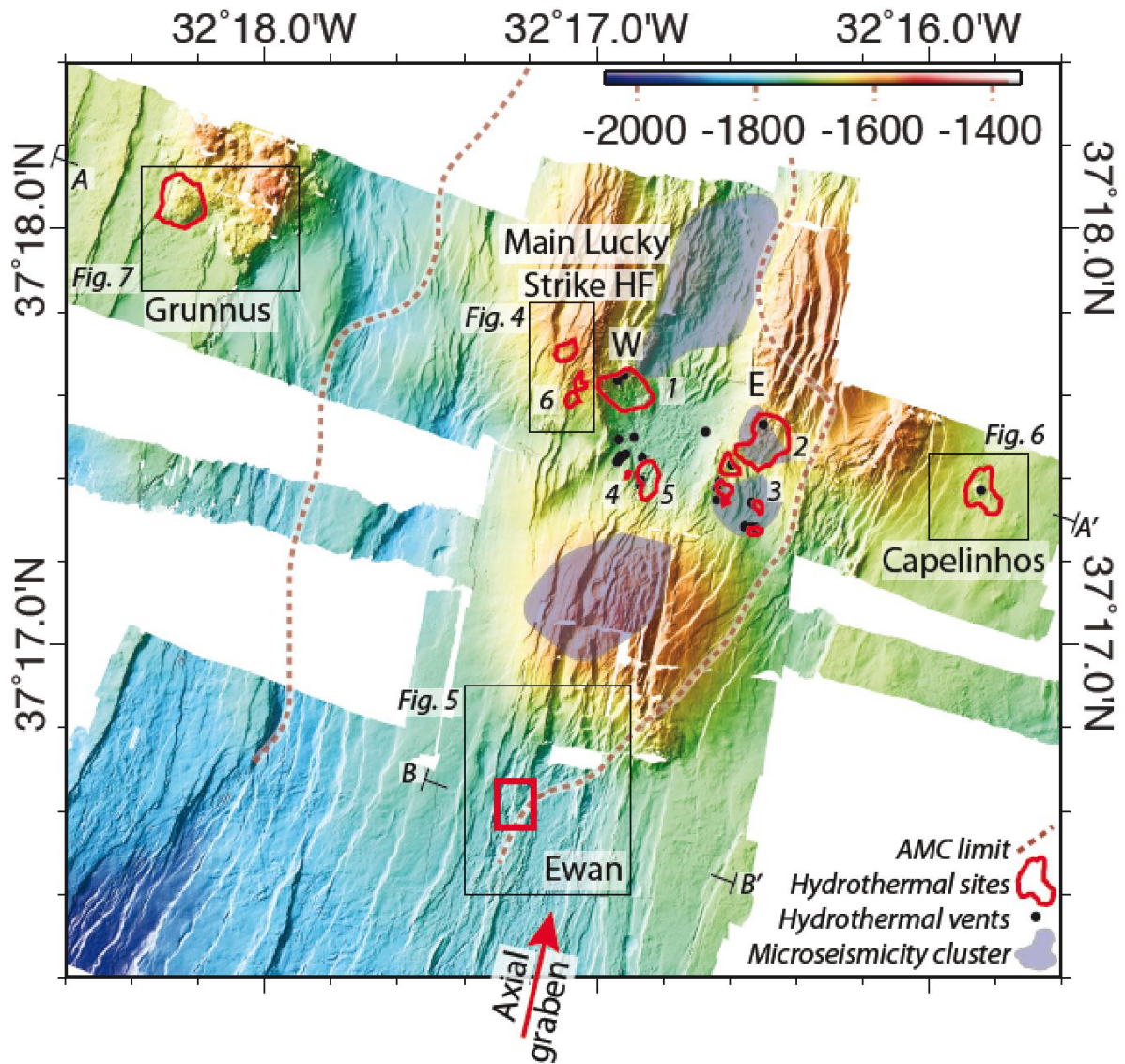
a) Lucky Strike Main Hydrothermal Field



b) Kilo Moana Hydrothermal Field (Lau Basin)

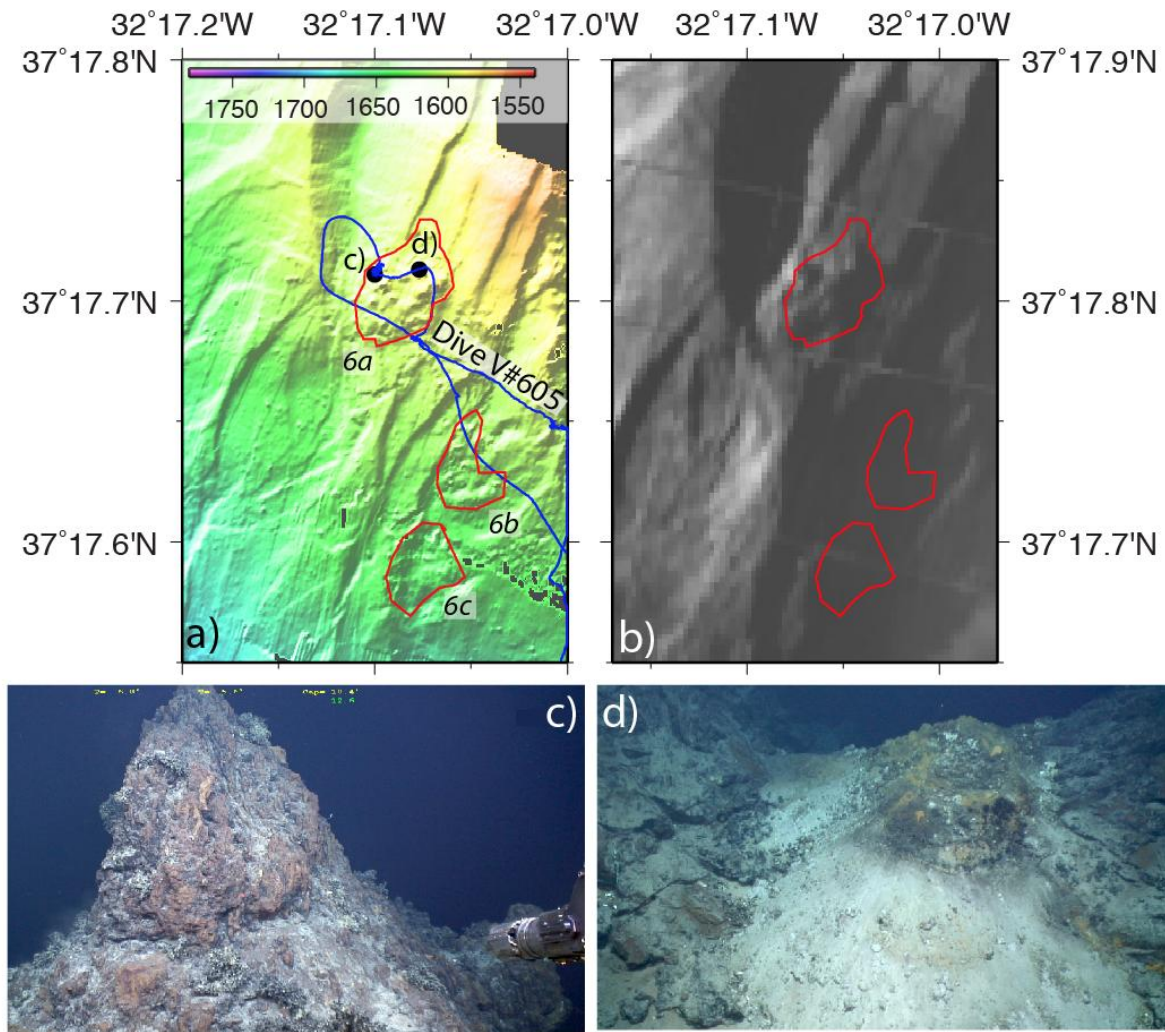
627

628 **Figure 2.** Perspective views showing the 'lumpy' seafloor morphology associated with
629 hydrothermal deposits described in the text. a) Microbathymetry from the Lucky Strike
630 Main Hydrothermal field, showing the ~20 m high Tour Eiffel (TE) vent and the
631 associated hydrothermal deposits around it, and smaller nearby vents (MS: Montsegur;
632 Ci: Cimendef). The view shows also several fault scarps and rubble on slopes, that are
633 morphologically distinct from hydrothermal deposits. b) Microbathymetry showing
634 hydrothermal vents in the Kilo Moana Hydrothermal Field in the Lau Basin (Ferrini et al.,
635 2008; Ferrini and Tivey, 2012), rising ~10-20 m above surrounding seafloor that is
636 faulted and fissured.



637

638 **Figure 3.** Microbathymetry of the Lucky Strike segment center showing the four
 639 hydrothermal fields identified and the present-day zone of accretion along the axial
 640 graben (red arrow). Red contours correspond to the limits of hydrothermal deposits
 641 identified in the microbathymetry, which are numbered for the Main Lucky Strike Field.
 642 The red square corresponds to the Ewan field, which lacks a geomorphologic signature,
 643 and black dots correspond to active vents. Boxes indicate the location of Figures 4
 644 through 7, and characteristics of fields are given in Table 1. The limits of the AMC (Singh
 645 et al., 2006; Combier et al., 2015) and location of microseismic clusters (Crawford et al.,
 646 2013) are also shown. A-A' and B-B' indicate endpoints of profiles shown in Figure 8a.



647

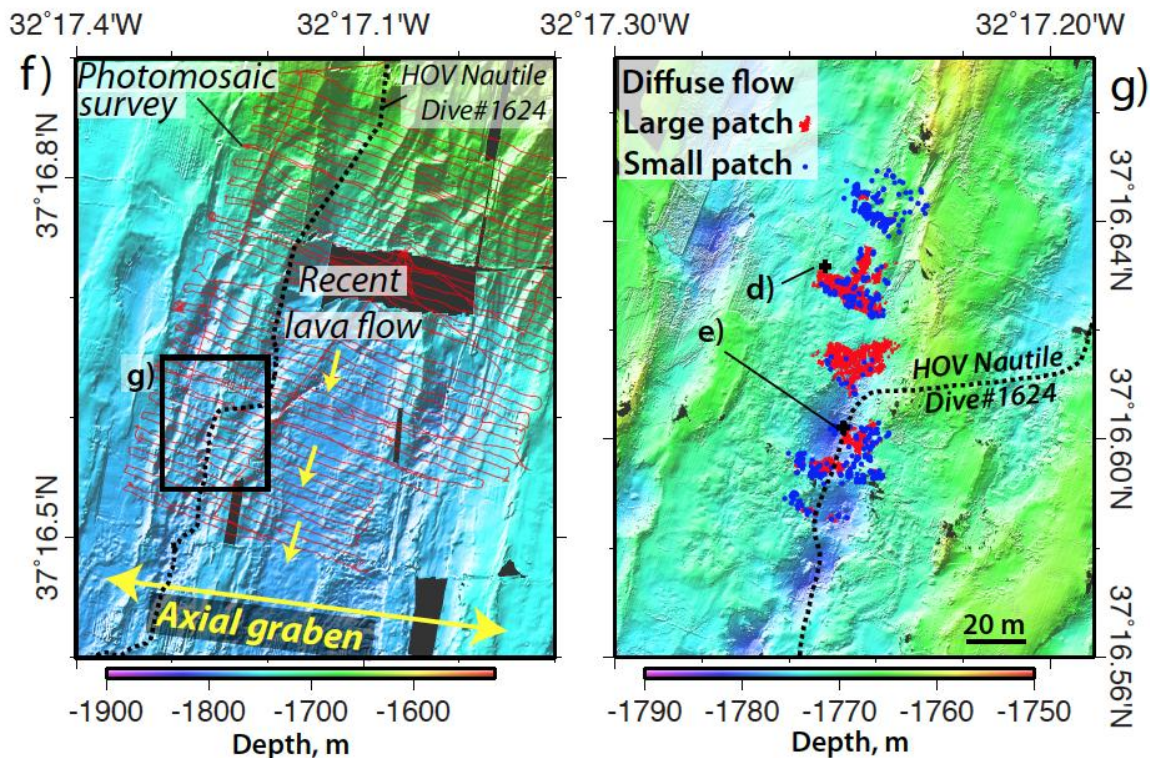
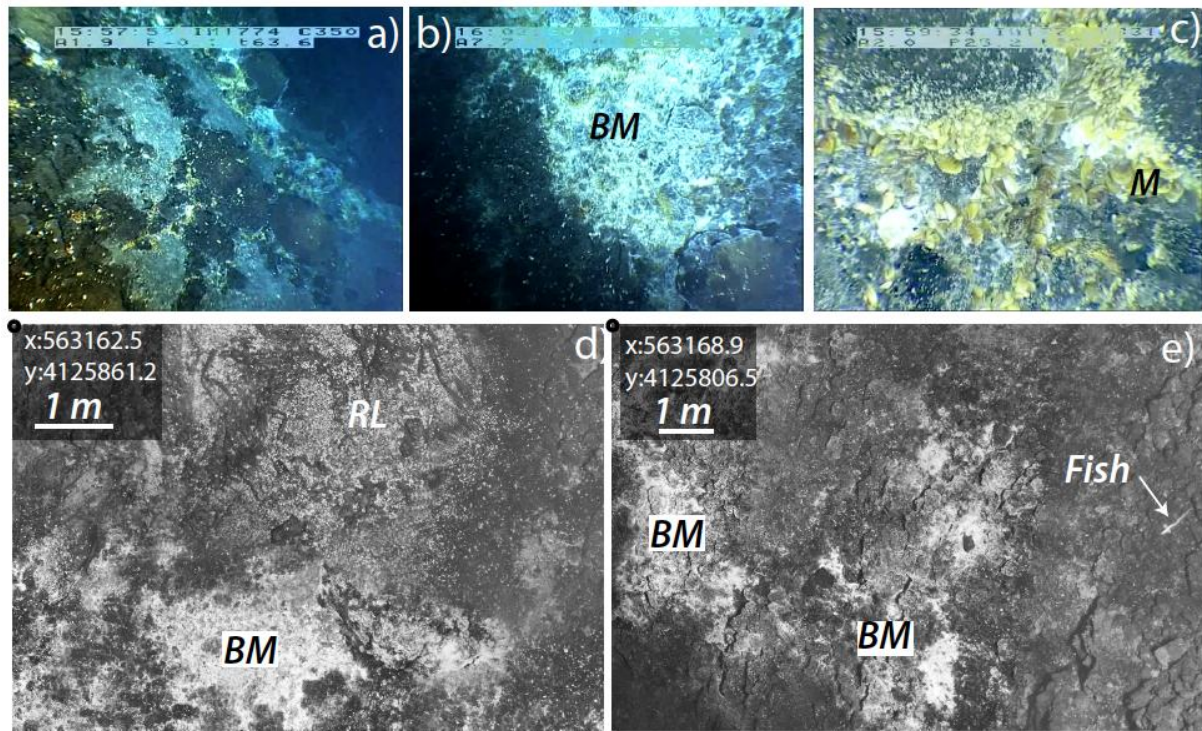
648

649 **Figure 4.** a) Microbathymetry of the western edge of the MLSHF, showing hydrothermal
 650 areas 6a-c in red (see Table 1 and Figure 3). c) and d) indicate the location of photos in
 651 Figures 4c and 4d, respectively. b) Acoustic backscatter image of the same area, with
 652 insonification from the west. Bright areas correspond to high backscatter, and black to
 653 acoustic shadows in this and following figures with sonar imagery. c) Inactive chimney
 654 and d) hydrothermal mound associated deposits observed during ROV VICTOR dive
 655 #605 (blue line).

656

657

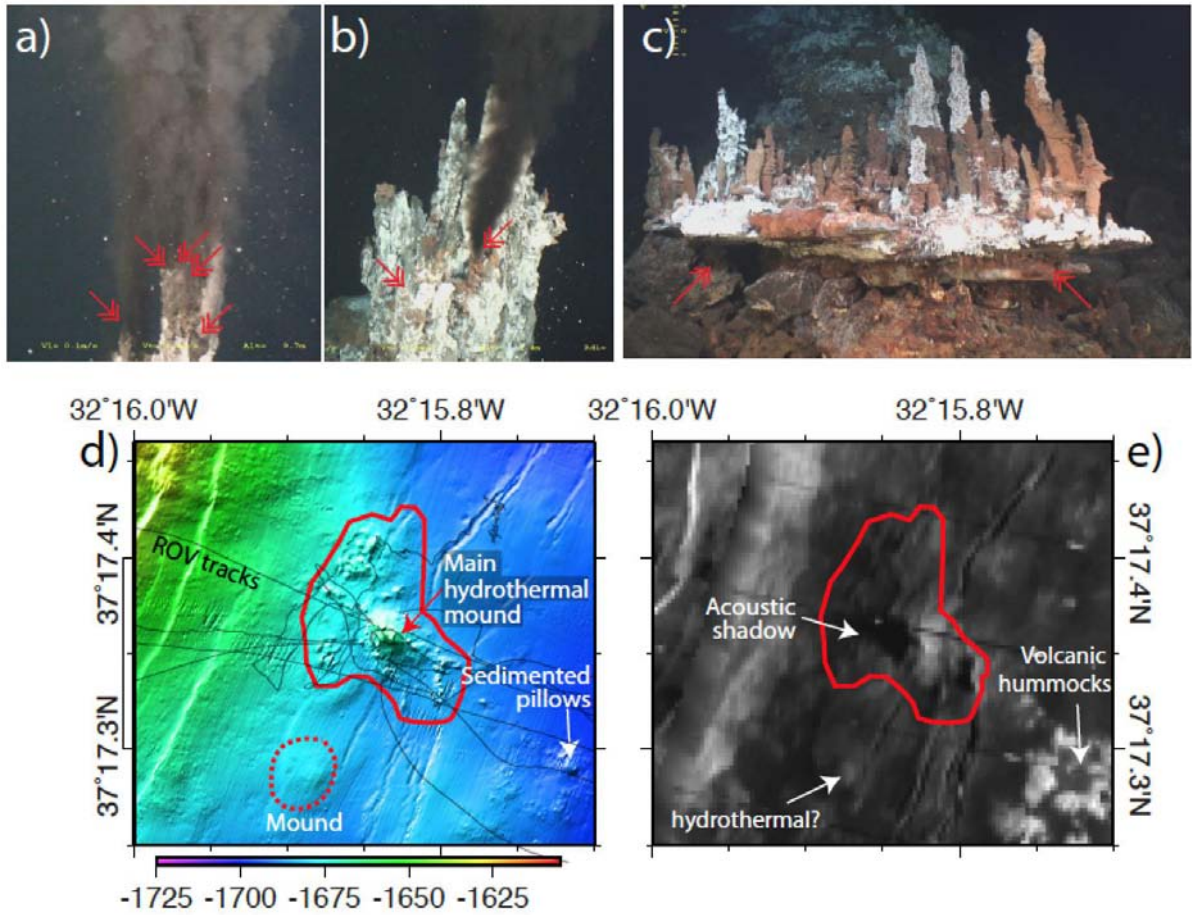
658



659

660 **Figure 5.** Ewan hydrothermal field. a)-c) Video grabs from HOV Nautilie dive #1616
 661 (Graviluck'06) show hydrothermal activity along steep slopes (a), with irregular patches
 662 of bacterial mats and diffuse flow through rubble (b), and associated with mussel beds
 663 (c). d) Vertical seafloor image mosaics (Bathyluck'09) showing patches of bacterial mats
 664 (BM) associated with diffuse flow extending over several meters over sedimented ropy
 665 lava flows (RL). e) Irregular bacterial mat patches, indicating localized diffuse outflow
 666 through steep scarps. Microbathymetry (50 cm/pixel) of the ridge axis on the southern
 667 flank of the rifted seamount south of the Main Lucky Strike field (f) and detail of the
 668 active zones (g). The coordinates of the top left corner of the photomosaics d) and e) are
 669 in UTM (m), and located in g).

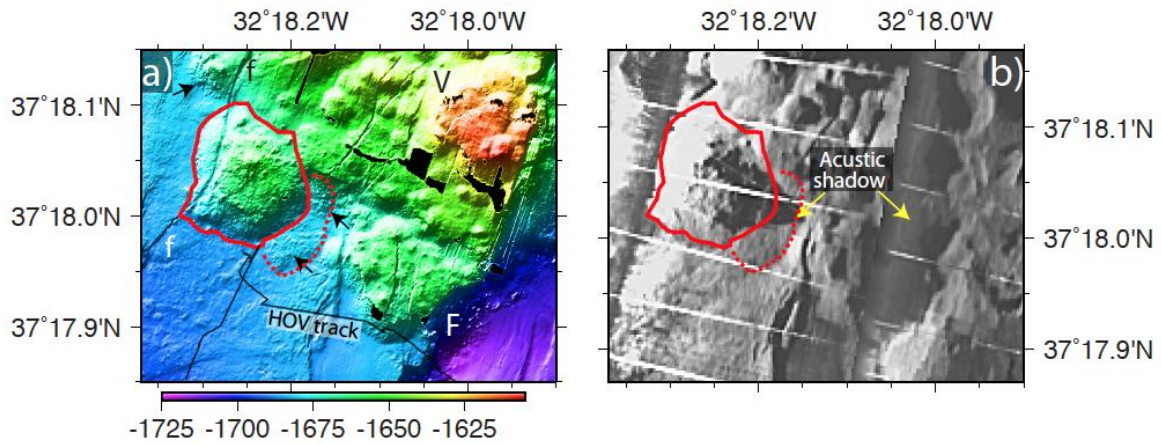
670



671

672 **Figure 6.** Capelinhos hydrothermal site. The main Capelinhos hydrothermal mound
 673 shows active chimneys with several black smoker vents (a-b) flanges with diffusers (c).
 674 Diffuse hydrothermal activity (bacterial mats) is scarce. d) Microbathymetry of the
 675 Capelinhos hydrothermal field (red outline), which displays a ~20 m high edifice
 676 emplaced over a set of small-scale faults and fissures, and a possible hydrothermal
 677 mound to the south (not visually inspected). e) Acoustic backscatter image with
 678 insonification from the E, showing the acoustic shadow of the edifice. The bathymetry
 679 reveals several mounds in surrounding areas (arrows); the structure to the SW has low
 680 acoustic backscatter and may correspond to another hydrothermal deposit. The
 681 structures to the SE are instead acoustically reflective and the sonar texture corresponds
 682 to volcanic hummocks.

683

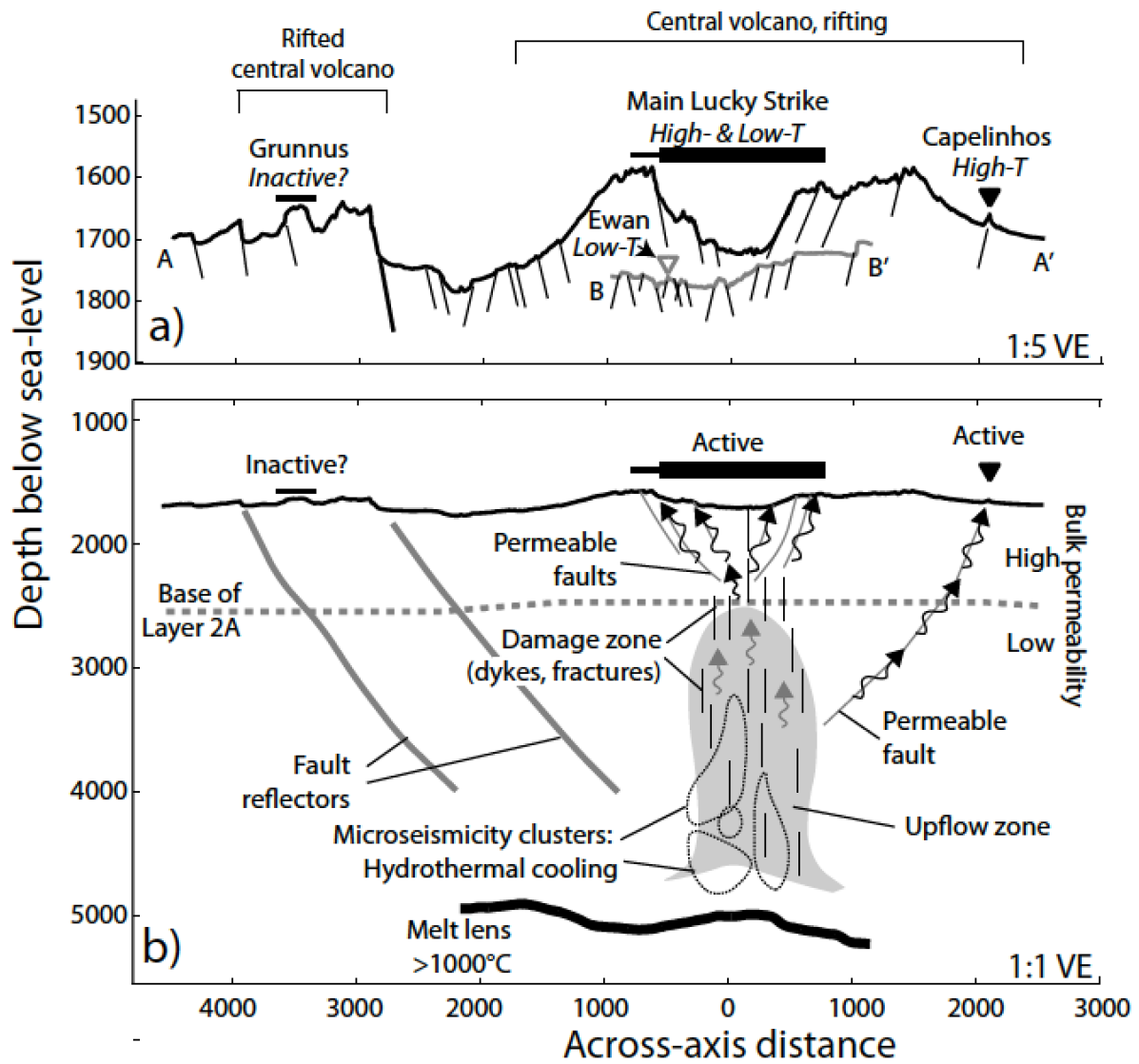


684

685

686 **Figure 7.** a) Microbathymetry of the Grunnus hydrothermal field (solid red line), and
 687 other possible hydrothermal structures (black arrows, dashed red line) located on the
 688 flank of a rifted central volcano (V, see Figure 3). A small normal fault (f) dissects the
 689 western flank of the ~200 meter diameter mound, while major fault (F) that dissects the
 690 central volcano can be linked to a fault seismic reflector to a depth of ~2 km below
 691 seafloor (Smith et al., 2006; Combier et al., 2015). b) Corresponding sonar imagery of the
 692 area.

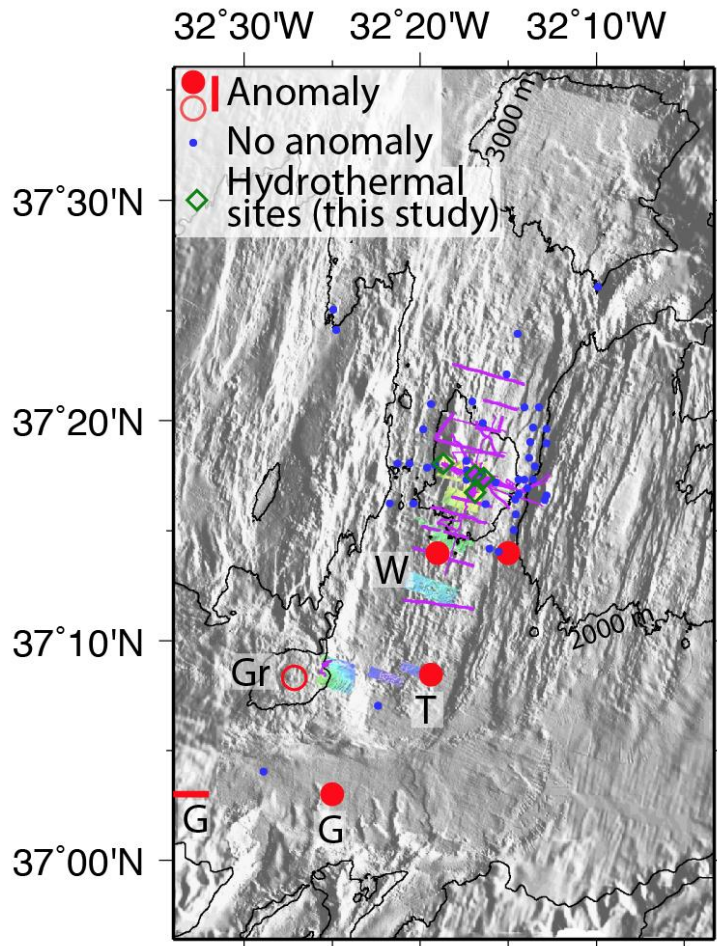
693



694

695 **Figure 8.** a) Microbathymetric profiles across the Grunnus-MLSHF-Capelinhos (black
 696 line) and across Ewan (grey line, see Figure 3 for location). b) Vertical cross-axis
 697 section of the crust showing the AMC and fault reflectors (Singh et al., 2006; Combiér et
 698 al., 2015) and the base of Layer 2A (Seher et al., 2010) from seismic data, and the
 699 projected positions of microseismicity clusters (Crawford et al., 2013). Hydrothermal
 700 upflow below Layer 2A is likely diffuse in the form of upwellings up to ~1 km in
 701 diameter (Fontaine et al., 2014) along the axis, which has a higher permeability due to
 702 damage induced by diking and cracking (Fontaine et al., 2014; Escartín et al., 2014). In
 703 the shallow crust hydrothermal outflow is likely channeled instead along permeable
 704 faults.

705



706

707 **Figure 9.**Map of the Lucky Strike field showing the location of water column
 708 nephelometry anomalies interpreted as indicators of hydrothermal plumes at depths of
 709 ~1800 m bsl (red), and hydrographic casts conducted during the Graviduck2006 cruise
 710 that yielded no anomalies (blue). Shaded relief is from shipboard bathymetry, the
 711 purple lines correspond to visual seafloor observations (Figure 1), the AUV and ROV
 712 microbathymetry is shown in color (see Figure 3), and sites described in this paper
 713 indicated by green diamonds. Water column anomalies: G: (German et al., 2006); T
 714 (Thurnherr et al., 2008); W (Wilson et al., 1996); Gr(Gràcia et al., 2000).

715 **References**

- 716 Baker, E.T., 2007, Hydrothermal cooling of mid ocean ridge axes: Do measured and
717 modeled heat fluxes agree? *Earth and Planetary Science Letters*, v. 263, p. 140–150.
- 718 Baker, E.T., Cormier, M.-H., Langmuir, C.H., and Zavala, K., 2001, Hydrothermal plumes
719 along segments of contrasting magmatic influence, 15°20'–18°30'N, East Pacific
720 Rise; Influence of axial faulting: *Geochemistry, Geophysics, Geosystems*, v. 2, p.
721 2000GC000165.
- 722 Barreyre, T., Escartín, J., Garcia, R., Cannat, M., Mittelstaedt, E., and Prados, R., 2012,
723 Structure, temporal evolution, and heat flux estimates from the Lucky Strike deep-
724 sea hydrothermal field derived from seafloor image mosaics: *Geochemistry,
725 Geophysics, Geosystems*, v. 13, no. 4, p. Q04007, doi: 10.1029/2011GC003990.
- 726 Barreyre, T., Escartin, J., Sohn, R., and Cannat, M., 2014a, Permeability of the Lucky Strike
727 deep-sea hydrothermal system: Constraints from the poroelastic response to ocean
728 tidal loading: *Earth and Planetary Science Letters*, v. 408, p. 146–154, doi:
729 10.1016/j.epsl.2014.09.049.
- 730 Barreyre, T., Escartín, J., Sohn, R.A., Cannat, M., Ballu, V., and Crawford, W.C., 2014b,
731 Temporal variability and tidal modulation of hydrothermal exit-fluid temperatures
732 at the Lucky Strike deep-sea vent field, Mid-Atlantic Ridge: *Journal of Geophysical
733 Research: Solid Earth*, v. 119, no. 4, p. 2543–2566, doi: 10.1002/2013JB010478.
- 734 Bischoff, J.L., and Seyfried, W.E., 1978, Hydrothermal chemistry of seawater from 25° to
735 350°C: *American Journal of Science*, v. 278, p. 838–860.
- 736 Bougault, H., Charlow, J.-L., Fouquet, Y., Needham, H.D., Vaslet, N., Appriou, P., Jean
737 Baptiste, P., Rona, P.A., Dmitriev, L., and Silantiev, S., 1993, Fast and slow-spreading
738 ridges: Structure and hydrothermal activity, ultramaphic topographic highs, and
739 CH₄ output: *Journal of Geophysical Research*, v. 98, no. B6, p. 9643–9651.
- 740 Charlou, J.-L., and Donval, J.-P., 1993, Hydrothermal methane venting between 12°N and
741 26°N along the Mid-Atlantic ridge: *Journal of Geophysical Research*, v. 98, no. B6, p.
742 9625–9642.
- 743 Colaço, A., Blandin, J., Cannat, M., Carval, T., Chavagnac, V., Connelly, D., Fabian, M.,
744 Ghiron, S., Goslin, J., Miranda, J.M., Reverdin, G., Sarrazin, J., Waldmann, C., and
745 Sarradin, P.-M., 2011, MoMAR-D: a technological challenge to monitor the dynamics
746 of the Lucky Strike vent ecosystem: *ICES Journal of Marine Science*, v. 68, no. 2, p.
747 416–424. doi:10.1093/icesjms/fsq075.
- 748 Combier, V., Seher, T., Singh, S.C., Crawford, W.C., Cannat, M., Escartín, J., and Dusunur, D.,
749 2015, Three-dimensional geometry of axial magma chamber roof and faults at
750 Lucky Strike volcano on the Mid-Atlantic Ridge: *Journal of Geophysical Research:
751 Solid Earth*, p. n/a–n/a, doi: 10.1002/2015JB012365.
- 752 Connelly, D.P., Copley, J.T., Murton, B.J., Stansfield, K., Tyler, P. a, German, C.R., Van Dover,
753 C.L., Amon, D., Furlong, M., Grindlay, N., Hayman, N., Hühnerbach, V., Judge, M., Le
754 Bas, T., et al., 2012, Hydrothermal vent fields and chemosynthetic biota on the
755 world's deepest seafloor spreading centre.: *Nature communications*, v. 3, p. 620,
756 doi: 10.1038/ncomms1636.

- 757 Crawford, W.C., Rai, A., Singh, S.C., Cannat, M., Escartín, J., Wang, H., Daniel, R., and
758 Combier, V., 2013, Hydrothermal seismicity beneath the summit of Lucky Strike
759 volcano, Mid-Atlantic Ridge: *Earth and Planetary Science Letters*, v. 373, p. 118–
760 128.
- 761 Crawford, W.C., Singh, S.C., Seher, T., Combier, V., Dusunur, D., Cannat, M., Rona, P.,
762 Devey, C.W., Dymont, J., and Murton, B., 2010, Crustal structure, magma chamber
763 and faulting beneath the Lucky Strike hydrothermal fields, *in* Diversity of
764 Hydrothermal Systems on Slow Spreading Ocean Ridges, AGU, Washington DC, p.
765 113–132.
- 766 Van Dover, C.L., German, C.R., Speer, K.G., Parson, L.M., and Vrijenhoek, R.C., 2002,
767 Evolution and Biogeography of Deep-Sea Vent and Seep Invertebrates: *Science*, v.
768 295, p. 1253–1257.
- 769 Dziak, R.P., Smith, D.K., Bohnenstiehl, D.R., Fox, C.G., Desbruyères, D., Matsumoto, H.,
770 Tolstoy, M., and Fornari, D.J., 2004, Evidence of a recent magma dike intrusion at the
771 slow spreading Lucky Strike segment, Mid-Atlantic Ridge: *Journal of Geophysical*
772 *Research*, v. 109, p. B12102, doi: 10.1029/2004JB003141.
- 773 Escartín, J., García, R., Delaunoy, O., Ferrer, J., Gracias, N., Elibol, A., Cufi, X., Fornari, D.J.,
774 Humphris, S.E., and Renard, J., 2008, Globally-aligned photo mosaic of the Lucky
775 Strike hydrothermal Vent Field (Mid-Atlantic Ridge, 37°18.5'N): release of geo-
776 referenced data, mosaic construction and viewing software: *Geochemistry,*
777 *Geophysics, Geosystems*, v. 9, no. 12, p. Q12009, doi:10.1029/2008GC002204.
- 778 Escartin, J., Garcia, R., Delaunoy, O., Ferrer, J., Gracias, N., Elibol, A., Cufi, X., Neumann, L.,
779 Fornari, D.J., Humphris, S.E., and Renard, J., 2008, Globally aligned photomosaic of
780 the Lucky Strike hydrothermal vent field (Mid-Atlantic Ridge, 37 degrees 18.50 ` N):
781 Release of georeferenced data, mosaic construction, and viewing software:
782 GEOCHEMISTRY GEOPHYSICS GEOSYSTEMS, v. 9, doi: 10.1029/2008GC002204.
- 783 Escartín, J., Soule, S.A., Cannat, M., Fornari, D.J., Düşünür, D., and Garcia, R., 2014, Lucky
784 Strike seamount: Implications for the emplacement and rifting of segment-centered
785 volcanoes at slow spreading mid-ocean ridges: *Geochemistry, Geophysics,*
786 *Geosystems*, v. 15, no. 11, p. 4157–4179, doi: 10.1002/2014GC005477.
- 787 Ferrini, V., and Tivey, M.K., 2012, ROV Jason 2 near-bottom multibeam bathymetry grids
788 from 6 vent fields in the Lau Back-arc Basin: *Integrated Earth Data Applications*
789 (IEDA), p. <http://doi.org/10.1594/IEDA/100028>.
- 790 Ferrini, V.L., Tivey, M.A., Carbotte, S.M., Martinez, F., and Roman, C., 2008, Variable
791 morphologic expression of volcanic, tectonic, and hydrothermal processes at six
792 hydrothermal vent fields in the Lau back-arc basin: *Geochemistry, Geophysics,*
793 *Geosystems*, v. 9, no. 7, p. Q07022, doi:10.1029/2008GC002047.
- 794 Fontaine, F.J., Cannat, M., Escartin, J., and Crawford, W.C., 2014, Along-axis hydrothermal
795 flow at the axis of slow spreading Mid-Ocean Ridges: Insights from numerical
796 models of the Lucky Strike vent field (MAR): *Geochemistry, Geophysics,*
797 *Geosystems*, v. 15, no. 7, p. 2918–2931, doi: 10.1002/2014GC005372.
- 798 Fontaine, F.J., Olive, J.A., Cannat, M., Escartin, J., and Perol, T., 2011,
799 Hydrothermally-induced melt lens cooling and segmentation along the axis of fast-

- 800 and intermediate-spreading centers: *Geophysical Research Letters*, v. 38, p. L14307,
801 doi:10.1029/2011GL047798.
- 802 Fouquet, Y., Charlou, J.L., Costa, I., Donval, J.P., Radford-Knoery, J., Pellé, H., Ondréas, H.,
803 Lourenço, N., Ségonzac, M., and Tivey, M.K., 1994, A detailed study of the Lucky
804 Strike hydrothermal site and discovery of a new hydrothermal site: Menez Gwen;
805 Preliminary results of the DIVAI Cruise (5-29 May, 1994): *InterRidge News*, v. 3, no.
806 2, p. 14–17.
- 807 German, C.R., Baker, E.T., Connelly, D.P., Lupton, J.E., Resing, J., Prien, R.D., Walker, S.L.,
808 Edmonds, H.N., and Langmuir, C., 2006, Hydrothermal exploration of the Fonualei
809 Rift and Spreading center and the Northeast Lau spreading center: *Geochemistry,*
810 *Geophysics, Geosystems*, v. 7, no. 11, p. Q11022, doi:10.1029/2006GC001324.
- 811 German, C.R., Parson, L.M., and Team, H.S., 1996, Hydrothermal exploration near the
812 Azores Triple Junction: tectonic control of venting at slow-spreading ridges: *Earth*
813 *and Planetary Science Letters*, v. 138, p. 93–104.
- 814 German, C.R., Thurnherr, A.M., Knoery, J., Charlou, J.L., Jean Baptiste, P., and Edmonds,
815 H.N., 2010, Heat, volume and chemical fluxes from submarine venting: A synthesis
816 of results from the Rainbow hydrothermal field, 361N MAR: *Deep-Sea Research I*, v.
817 57, p. 518–527.
- 818 Gràcia, E., Charlou, J.L., Radford-Knoery, J.R., and Parson, L.M., 2000, Non-transform
819 offsets along the Mid-Atlantic Ridge south of the Azores (38°N–34°N): Ultramafic
820 exposures and hosting of hydrothermal vents: *Earth and Planetary Science Letters*,
821 v. 177, p. 89–103.
- 822 Gràcia, E., Parson, L.M., Bideau, D., and Hekinian, R., 1998, Volcano-tectonic variability
823 along segments of the Mid-Atlantic Ridge between the Azores platform and Hayes
824 fracture zone: Evidence from submersible and high-resolution side-scan sonar data,
825 *in* Mills, R.A. and Harrison, K. eds., *Modern ocean floor processes and the geological*
826 *record*, Geological Society, London, p. 1–15.
- 827 Haase, K.M., Koschinsky, A., Petersen, T., Devey, C.W., German, C., Lackschewitz, K.S.,
828 Melchert, B., Seifert, R., Borowski, C., Giere, O., and Paulick, H., 2009, Diking, young
829 volcanism and diffuse hydrothermal activity on the southern Mid-Atlantic Ridge:
830 The Lilliput field at 9°33'S: *Marine Geology*, v. 266, p. 52–64.
- 831 Haymon, R.M., Macdonald, K.C., Benjamin, S.B., and Ehrhardt, C.J., 2005, Manifestations of
832 hydrothermal discharge from young abyssal hills on the fast-spreading East Pacific
833 Rise flank: *Geology*, v. 33, p. 153–156; doi: 10.1130/G21058.1.
- 834 Humphris, S.E., Fornari, D.J., Scheirer, D.S., German, C.R., and Parson, L.M., 2002,
835 Geotectonic setting of hydrothermal activity on the summit of Lucky Strike
836 seamount (37°17'N, Mid-Atlantic Ridge): *Geochemistry, Geophysics, Geosystems*, v.
837 3, no. 8, p. 10.1029/2001GC000284.
- 838 Humphris, S.E., and Kleinrock, M.C., 1996, Detailed morphology of the TAG active
839 hydrothermal mound: Insights into its formation and growth: *Geophysical Research*
840 *Letters*, v. 23, no. 23, p. 3443–3446.

- 841 Jamieson, J.W., Clague, D. a., and Hannington, M.D., 2014, Hydrothermal sulfide
842 accumulation along the Endeavour Segment, Juan de Fuca Ridge: *Earth and*
843 *Planetary Science Letters*, v. 395, p. 136–148, doi: 10.1016/j.epsl.2014.03.035.
- 844 Karson, J.A., and Brown, J.R., 1988, Geologic setting of the Snake Pit hydrothermal site:
845 an active vent field on the Mid-Atlantic Ridge: *Marine Geophysical Researches*, v. 10,
846 p. 91–107.
- 847 Kelley, D.S., Delaney, J.R., and Juniper, S.K., 2014, Establishing a new era of submarine
848 volcanic observatories: Cabling Axial Seamount and the Endeavour Segment of the
849 Juan de Fuca Ridge: *Marine Geology*, v. 352, p. 426–450, doi:
850 10.1016/j.margeo.2014.03.010.
- 851 Kleinrock, M.C., Humphris, S., and Thompson, G., 1993, Relations between volcanism,
852 tectonism and hydrothermalism along the TAG segment of the Mid-Atlantic ridge:
853 WHOI.
- 854 Klinkhammer, G., Rona, P., Greaves, M., and Elderfield, H., 1985, Hydrothermal
855 manganese plumes in the Mid-Atlantic Ridge rift valley: *Nature*, v. 314, p. 727–731.
- 856 Lalou, C., Brichet, E., and Lange, J., 1989, Fossil hydrothermal sulfide deposits at the
857 Galapagos Spreading Centre near 85°00 West: geological setting, mineralogy and
858 chronology: *Oceanologica acta*, v. 12, no. 1, p. 1–8.
- 859 Langmuir, C., Humphris, S., Fornari, D., Van Dover, C., Von Damm, K., Tivey, M.K.,
860 Colodner, D., Charlou, J. -l., Desonie, D., Wilson, C., Fouquet, Y., Klinkhammer, G., and
861 Bougault, H., 1997, Hydrothermal vents near a mantle hot spot: the Lucky Strike
862 vent field at 37°N on the Mid-Atlantic Ridge: *Earth and Planetary Science Letters*, v.
863 148, p. 69–91.
- 864 Lupton, J., 1990, Water column hydrothermal plumes on the Juan de Fuca Ridge: *Journal*
865 *of Geophysical Research*, v. 95, no. B8, p. 12829–12842.
- 866 Marcon, Y., Sahling, H., Borowski, C., dos Santos Ferreira, C., Thal, J., and Bohrmann, G.,
867 2013, Megafaunal distribution and assessment of total methane and sulfide
868 consumption by mussel beds at Menez Gwen hydrothermal vent, based on geo-
869 referenced photomosaics: *Deep Sea Research Part I: Oceanographic Research*
870 *Papers*, v. 75, p. 93–109, doi: 10.1016/j.dsr.2013.01.008.
- 871 Mittelstaedt, E., Escartín, J., Gracias, N., Olive, J.-A., Barreyre, T., Davaille, A., Cannat, M.,
872 and Garcia, R., 2012, Quantifying diffuse and discrete venting at the Tour Eiffel vent
873 site, Lucky Strike hydrothermal field: *Geochemistry Geophysics Geosystems*, v. 13,
874 no. 4, p. Q04008, doi: 10.1029/2011GC003991.
- 875 Murton, B.J., Klinkhammer, G., Becker, K., Briais, A., Edge, D., Hayward, N., Millard, N.,
876 Mitchell, I., Rousse, I., Rudnicki, J.W., Sayanagi, K., Sloan, H., and Parson, L., 1994,
877 Direct evicence for the distribution and occurrence of hydrothermal activity
878 between 27°N -30°N on the Mid-Atlantic Ridge: *Earth and Planetary Science Letters*,
879 v. 125, p. 119–128.
- 880 Murton, B.J., Redbourn, L.J., German, C.R., and Baker, E.T., 1999, Sources and fluxes of
881 hydrothermal heat, chemicals and biology within a segment of the Mid-Atlantic
882 Ridge: *Earth and Planetary Science Letters*, v. 171, p. 301–317.

- 883 Olafsson, J., Honjo, S., Thors, K., Stefansson, U., Jones, R.R., and Ballard, R.D., 1989, Initial
884 observations, bathymetry and photography of a geothermal site on the Kolbeinsey
885 Ridge, *in* *Oceanography 1988 : JOA Mexico* 88, p. 121–127.
- 886 Ondreas, H., Cannat, M., Fouquet, Y., Normand, A., Sarradin, P.M., and Sarrazin, J., 2009,
887 Recent volcanic events and the distribution of hydrothermal venting at the Lucky
888 Strike hydrothermal field, Mid-Atlantic Ridge: *GEOCHEMISTRY GEOPHYSICS*
889 *GEOSYSTEMS*, v. 10, doi: 10.1029/2008GC002171.
- 890 Ondréas, H., Cannat, M., Fouquet, Y., Normand, A., Sarradin, P.-M., and Sarrazin, J., 2009,
891 Recent volcanic events and the distribution of hydrothermal venting at the Lucky
892 Strike hydrothermal field, Mid-Atlantic Ridge: *Geochemistry, Geophysics,*
893 *Geosystems*, v. 10, no. 2, p. Q02006, doi:10.1029/2008GC002171.
- 894 Ondreas, H., Fouquet, Y., Voisset, M., and Radford-Knoery, J., 1997, Detailed study of
895 three contiguous segments of the Mid-Atlantic Ridge, South of the Azores (37°N to
896 38°30'N), using acoustic imaging coupled with submersible observations: *Marine*
897 *Geophysical Researches*, v. 19, p. 231–255.
- 898 Pedersen, R.B., Thorseth, I.H., Nygård, T.E., Lilley, M., and Kelley, D.S., 2010,
899 Hydrothermal Activity at the Arctic Mid-Ocean Ridges, *in* Rona, P., Devey, C.W.,
900 Dymont, J., and Murton, B. eds., *Diversity of Hydrothermal Systems on Slow*
901 *Spreading Ocean Ridges*, p. 67–89.
- 902 Prados, R., Garcia, R., Gracias, N., Escartín, J., and Neumann, L., 2012, A novel blending
903 technique for underwater gigamosaicing: *IEEE Journal of Oceanic Engineering*, v.
904 37, no. 4, p. 10.1109/JOE.2012.2204152.
- 905 Scheirer, D.S., Fornari, D.J., Humphris, S.E., and Lerner, S., 2000, High-resolution seafloor
906 mapping using the DSL-120 sonar system: Quantitative assessment of sidescan and
907 phase-bathymetry data from the Lucky Strike segment of the Mid-Atlantic Ridge:
908 *Marine Geophysical Researches*, v. 21, p. 121–142.
- 909 Seher, T., Crawford, W.C., Singh, S.C., and Cannat, M., 2010, Seismic layer 2A variations in
910 the Lucky Strike segment at the Mid-Atlantic Ridge from reflection measurements:
911 *Journal of Geophysical Research*, v. 115, p. B07107, doi:10.1029/2009JB006783.
- 912 Singh, S.C., Crawford, W.C., Carton, H., Seher, T., Combier, V., Cannat, M., Canales, J.P.,
913 Düsünür, D., Escartín, J., and Miranda, J., 2006, Discovery of a magma chamber and
914 faults beneath a Mid-Atlantic Ridge hydrothermal field: *Nature*, v. 442, p. 1029–
915 1032.
- 916 Smith, D.K., and Cann, J.R., 1990, Hundreds of small volcanoes on the median valley floor
917 of the Mid-Atlantic Ridge: *Nature*, v. 344, p. 427–431.
- 918 Smith, D.K., Cann, J.R., and Escartín, J., 2006, Widespread active detachment faulting and
919 core complex formation near 13°N on the Mid-Atlantic Ridge: *Nature*, v. 443, p.
920 440–444, doi:10.1038/04950.
- 921 Thurnherr, A.M., Reverdin, G., Bouruet-Aubertot, P., St. Laurent, L.C., Vangriesheim, A.,
922 and Ballu, V., 2008, Hydrography and flow in the Lucky Strike segment of the Mid-
923 Atlantic Ridge: *Journal of Marine Research*, v. 66, p. 347–372.

- 924 Wilson, C., Charlou, J.-L., Ludford, E., Klinkhammer, G., Chin, C., Bougault, H., German, C.,
925 Speer, K., and Palmer, M., 1996, Hydrothermal anomalies in the Lucky Strike
926 segment on the Mid-Atlantic Ridge (37°17'N): Earth and Planetary Science Letters,
927 v. 142, p. 467–477.
- 928 Yeo, I., Searle, R.C., Achenbach, K.L., Le Bas, T.P., and Murton, B.J., 2011, Eruptive
929 hummocks: Building blocks of the upper ocean crust: *Geology*, v. 40, no. 1, p. 91–94,
930 doi: 10.1130/G31892.1.
- 931